Journal of the European Ceramic Society, **2016**, *36*, 89-100.

Influence of excesses of volatile elements on structure and composition of solution derived lead-free $(Bi_{0.50}Na_{0.50})_{1-x}Ba_xTiO_3$ thin films

Pérez-Mezcua D[a], Calzada M L[a], Bretos I[a], Ricote J[a], Jiménez R[a], Fuentes- Cobas L[b], Escobar-Galindo R[a] Chateigner D[c], Sirera R[d,*]

[a]Instituto de Ciencia de Materiales de Madrid (ICMM), C.S.I.C., 28049 Cantoblanco-Madrid, Spain

[b]Centro de Investigación en Materiales Avanzados, 31109 Chihuahua, Mexico

[c]CRISMAT-ENSICAEN and IUT-Caen, Université de Caen Basse-Normandie, 14050 Caen, France

[d]Departamento de Química y Edafología, Facultad de Ciencias, Universidad de Navarra, 31008 Pamplona, Spain

*Corresponding author. E-mail address: rsirera@unav.es (R. Sirera)

Abstract

The preparation of $(Bi_{0.50}Na_{0.50})_{1-x}Ba_xTiO_3$ films requires a compositional/structural control, as they determine the functionality of these materials. We report a systematic compositional and structural analysis on $(Bi_{0.50}Na_{0.50})_{1-x}Ba_xTiO_3$ films fabricated by chemical solution deposition. The effects of incorporating Na(I) and Bi(III) excesses are analyzed through the comparison of the compositional depth profiles of stoichiometric films (BNBT) and films containing excesses (BNBTxs). Heterogeneous compositional profiles with larger bismuth content close to the substrate and thicker film-substrate interfaces are observed in BNBTxs, unlike stoichiometric films, which show atomic concentrations that correspond to the nominal composition of the precursor solution. Excesses induce structural differences in depth, observing a shift of the region of coexistence of rhombohedral and tetragonal phases (morphotropic phase boundary) towards higher x values and the formation of thick film-substrate interfaces. In contrast, stoichiometric films have homogeneous compositional and structural profiles with the MPB placed close to that described for bulk ceramics.

Keywords. thin film; lead-free; perovskite; morphotropic phase boundary; chemical solution deposition;

Introduction

High performance piezoelectric ceramics, which are widely used in micro- and nano-electromechanical systems (MEMS and NEMS), are mainly based on the lead zirconate titanate $Pb(Zr_xTi_{1-x})O_3$, (PZT) [1, 2]. The main concern over the use of this material is its environmental impact, related to the pollutant lead content. Thus, the search of lead-free alternatives is attracting much attention [3-5].

Among the lead-free materials, $(Bi_{0.5}Na_{0.5})TiO_3$ (BNT) [6] is an example of a distorted perovskite where the charge difference between sodium and bismuth cations is large enough to provide an energy ordering in the system. This results in a complex nano-domain structure, which confers it a particular electric response [7].

The main drawbacks of BNT, which limit its applications, are the high conductivity and coercive field. These make difficult the poling process and thus, modified BNT compositions are being used [8]. Among them, $(Bi_{0.5}Na_{0.5})_{1-x}Ba_xTiO_3$ (BNBT) is considered an attractive system to be studied as it presents a morphotropic phase boundary (MBP), similarly to PZT, where the electromechanical properties are maximized [9].

The MPB can be defined as the composition at which a phase transition occurs between two adjacent crystalline phases that have equal Gibbs free energy [10]. The optimization of the ferro-piezoelectric properties at the MPB of BNBT was originally explained by the coexistence of tetragonal and rhombohedral phases [11]. However, the phase transformation seems to be promoted not only by the composition but also by the temperature or even by an electric field; in this way the MPB in BNBT materials could be modified during the poling process [12, 13]. It has been reported that the phase transition at the MPB occurs through intermediate phases of monoclinic symmetry [14,15]. Furthermore, recently the structures observed at long-range order have been found to be different from those detected at short-range order (nano-scale) in nanostructured BNBT ceramics [16], which shows the complexity of the crystallographic structure of these compositions.

Besides, it has been reported that for compositions with x between 0.055 and 0.12 the BNBT solid solution exhibits a variety of different crystalline structures. This has caused some controversy, that has not been settled fully yet. For compositions between x ~0.06 and x ~0.10, a cubic phase ($Pm\bar{3}m$ space group) is determined by X-ray diffraction for unpoled BNBT [17,18]. This cubic structure is described as a multiphase system, which at short-range order is constituted by tetragonal nano-regions (P4bm space group) with antiferroelectric or ferroelectric response, and ferroelectric rhombohedral regions (R3c space group). This structural model is in agreement with the relaxor-ferroelectric behavior reported in the literature for these materials [19]. However, according to Jo et al, a structural evolution from rhombohedral R3c/R3m to tetragonal P4mm occurs in the compositional range of $0.055<x<0.100$ [20]. Free energies of these crystalline structures are very similar; thus, in BNBT bulk materials with close nominal compositions, different crystalline structures can be found. If the determination of crystalline structures seems not to be clarified in bulk materials, it becomes a challenge in polycrystalline thin films.

The need to integrate this lead-free piezoelectric material in microelectronic devices makes the fabrication of thin films essential. The high compositional control required to obtain films with compositions close to the MPB in these complex oxides makes chemical solution deposition (CSD) one of the most appropriate techniques to fabricate BNBT thin films [21]. For the processing it must be taken into account that the BNBT solid solution contains two elements of high volatility, Na(I) and Bi(III). Their loss by volatilization during any of the thermal processes needed in CSD disrupts the compositional balance of the thin films. In principle, high volatilization rates are

expected due to the high surface/volume ratio inherent in thin films. Traditionally excesses of these two volatile elements are incorporated in the precursor solutions to compensate the loss during the films annealing [22-25]. It has been reported that the use of these excesses produces displacements of the MPB position for thin films [25] but the associated compositional and structural changes that lead to this shift are poorly understood.

Here, we show our recent results in solution derived $(Bi_{0.50}Na_{0.50})_{1-x}Ba_xTiO_3$ thin films, concerning the effects on their composition and crystalline structure produced by the use of Na(I) and Bi(III) excesses in the precursor. At the same time, we explore in depth the diversity of crystalline phases present in these films with compositions around the MPB. The study is carried out by Rutherford Backscattering Spectroscopy and X-ray diffraction for a wide range of x values (with x from 0.035 to 0.150), including those reported as being in the MPB region for bulk ceramics. The structure of the $(Bi_{0.50}Na_{0.50})_{1-x}Ba_xTiO_3$ thin films is studied in comparison with their counterpart bulk ceramics prepared following an identical chemical route. The complexity of these analysis and the interest of getting information about the structural profiles of the films have required the use of Grazing-incidence X-ray diffraction (GIXRD) with synchrotron radiation. New insights on the peculiarities of the crystalline characteristics of polycrystalline BNBT thin films arise from the discussion of the results of this work.

Experimental Procedure

Details of the synthesis for $(Bi_{0.50}Na_{0.50})_{1-x}Ba_xTiO_3$ precursor solutions can be found elsewhere [22, 26]. It can be summarized as follows: $(Bi_{0.50}Na_{0.50})_{1-x}Ba_xTiO_3$ precursor solutions were synthesized by a hybrid route. Solutions with the stoichiometric nominal compositions and different Ba(II) contents (x=0.035, 0.055 and 0.100) were prepared; they are denoted as BNBT3.5, BNBT5.5 and BNBT10.0, respectively. Similarly, $(Bi_{0.55}Na_{0.55})_{1-x}Ba_xTiO_{3.30}$ nominal solutions containing a 10 mol% excess of Na(I) and a 10 mol% excess of Bi(III), and with different concentrations of Ba(II) (x=0.055, 0.100, 0.150), hereinafter BNBTxs5.5, BNBTxs10.0 and BNBTxs15.0, were also synthesized.

Diluted solutions (0.20 M) in dried ethanol were deposited onto $Pt/TiO_2/SiO_2/(100)Si$ substrates (Radiant Technologies) by spin coating at 2000 rpm for 45 s and dried at 350^{o}C for 60s, in a hot plate. The as-deposited amorphous films were crystallized by rapid thermal processing (RTP, JetStar 100T JIPELEC) in an oxygen atmosphere at 650^{o}C for 60 s (heating rate of 30^{o}C s^{-1}). Deposition, drying and crystallization were repeated six times. Compositions of the $(Bi_{0.50}Na_{0.50})_{1-x}Ba_xTiO_3$ films were selected (i) for x values lower than the MPB region; (ii) for x values inside the MPB region, and (iii) for x values higher than the MPB region; that means x= 0.035, 0.050 and 0.100 for BNBT films and x= 0.055, 0.100 and 0.150 for BNBTxs films [19, 26].

In addition to BNBT stoichiometric and BNBTxs thin films, containing 10mol% excess of Na(I) and Bi(III), BNBT stoichiometric bulk ceramics were studied. For the preparation of bulk ceramics which are taken as a reference, the same solutions with the stoichiometric nominal compositions for x=0.035, 0.055 and 0.100 were used.

Significant losses of volatiles elements are not expected during annealing of bulk ceramics, therefore Na(I) and Bi(III) excesses were not used here [17,18]. The solutions were dried at 120^{o}C for 12h in air. The gels were heated at 350^{o}C in air for 12h and subsequently annealed at 800^{o}C for 2h (heating rate 2^{o}C·min^{-1}). The powders were mixed with 2-propanol ($(CH_3)_2CHOH$, Aldrich, 99.5%) used as a binder, and were pressed into discs of 10 mm of diameter and 2 mm of thickness. The green ceramics were sintered in air at 1100^{o}C for 2h (heating rate 2^{o}C·min^{-1}). The bulk density of the resulting ceramics were determined by the Archimedes method. The calculated values were 5.62 g·cm^{-3} (densification of 94.9%), 5.83 g·cm^{-3} (densification of 98.5%) and 5.72 g·cm^{-3} (densification of 96.6%) for the BNBT3.5, BNBT5.5 and BNBT10.0 bulk ceramics, respectively.

Rutherford Backscattering Spectroscopy (RBS) experiments were performed to analyze the compositional depth profile of the films. A 5 MV HVEE Tandetron accelerator was used with a 2 MeV He^{+} beam. The data were acquired with a silicon surface barrier detector located at a scattering angle of 170°, with an energy resolution of 16 keV at an ion dose of 10 μC. The experimental spectra were fitted with the software RBS [27].

Plan-view and cross-section micrographs of the crystalline oxide films were obtained by field-emission gun scanning electron microscopy (FEG-SEM, Nova Nanosem 230 FEI Company equipment, Hillsboro, OR).

The crystalline phases were initially studied using a Siemens D500 powder diffractometer with a Cu anode and a Bragg-Brentano geometry. Diffraction patterns of the bulk ceramics were measured in the 2θ interval between 20^{o} and 50^{o}, with a step of 0.05^{o} per each 3s. More detailed patterns were recorded in the 2θ intervals between 37.0-42.0^{o} and 46.0-47.5^{o}, using a step of 0.005º per each 5s. These patterns were analyzed with the V1-40 program. Peaks of the patterns were separated and fitted to pseudo-Voigt 2 functions.

The crystalline structure developed in the films was studied using a four-circle diffractometer equipped with a closed Eulerian goniometer (χ, φ), a Cu anode, a 120° curve linear position-sensitive detector (CPS120 from INEL SA) and a flat graphite primary monochromator. XRD patterns of 120° in 2θ were recorded in a regular grid of 5°×5° in χ and φ, with χ from 0° to 50° and φ from 0° to 355° (a total of 864 patterns). Rietveld refinement calculations were carried out with the Materials Analysis Using Diffraction Package (MAUD) [28]. The refinements were performed on the patterns resulting from the sum of the collected ones for each angular position (χ, φ), in order to analyze a randomized pattern of the films. The random texture model has been selected for carrying out the simulations of the experimental patterns, since changes of the intensity of the perovskite peaks with the angular position have not been observed. Two layers were included for the fitting: (i) a perovskite layer containing a R3c rhombohedral and/or P4mm tetragonal structure and (ii) a Pt substrate layer with a cubic structure ($Fm\bar{3}m$).

Grazing-incidence X-ray diffraction (GIXRD) was carried out at the beamline 11-3 of the Stanford Synchrotron Radiation Lightsource (Stanford, USA). A MAR345 two-dimensional (2D) position-sensitive detector was used with a sample-detector distance

of 180 mm. The 2D diffraction patterns were recorded using a X-ray wavelength of λ=0.9744 Å and incidence angles of 0.05° and 0.15° to study the structural changes at different depth of the BNBT5.5 and BNBTxs10.0 films. Experimental 1D patterns were obtained by integration of the Debye rings processed by the software Fit-2D and the phases fractions as well as the cell sizes were refined with the software Fullprof. 2D intensity data have not been corrected before the integration with Fit2D.

Results

In this work, three sets of samples were studied: (i) BNBT stoichiometric thin films, (ii) BNBTxs thin films, containing 10mol% excess of Na(I) and Bi(III), and (iii) BNBT stoichiometric bulk ceramics (significant losses of volatile elements are not expected during annealing of bulk ceramics, therefore Na(I) and Bi(III) excesses were not used here) [17, 18].

Figure 1 and Figure 2 show the average of atoms per cell across the film (a-c) and the corresponding experimental and fitted RBS curves (d-f) for the BNBT and BNBTxs thin films, respectively. Simulations of the experimental RBS data allow us to gain a deep knowledge of the compositional depth profile in the films. The calculated data from the RBS spectra are shown in Table I. They reveal three differentiated zones/layers across the films: (i) a bismuth deficient layer on the surface, (ii) a bulk layer with a composition close to that of the nominal composition of the precursor solution, considering the composition of the $(Bi_{0.55}Na_{0.55})_{1-x}Ba_xTiO_{3.30}$ (for BNBTxs) or $(Bi_{0.50}Na_{0.50})_{1-x}Ba_xTiO_3$ (for BNBT) solid solution, and (iii) a bottom interface formed by the interaction between the film and the Pt-coated substrate. Film thickness has also been calculated from the RBS data, considering the density of the perovskite obtained from the resolved unit cells by Rietveld refinement of the X-ray patterns shown in Table II. For the BNBT3.5, BNBT5.5 and BNBT10.0 films, the average composition per atom (value normalized to the nominal composition of the $(Bi_{0.50}Na_{0.50})_{1-x}Ba_xTiO_3$ perovskite) in the bulk layer, calculated from the simulation, is x ~0.035, ~0.055 and ~0.100. They are practically identical to the nominal solid solution composition (Table I). Most of the film thickness (~90 % calculated value for the three films) presents the nominal composition, which proves the compositional homogeneity achieved without the introduction of any excess in the precursor solution. In addition, these BNBT films exhibit a rapid increase in the intensity of the signal around 1400 keV, which corresponds to the scattering cross section of the platinum (Figure 1 d-f), and can be associated with an abrupt film/substrate interface. The calculated thickness of these Bi_xPt interfaces is <6% for the three BNBT films, which is associated with a low degree of interdiffusion between the film and the Pt electrode. A thin bismuth deficient layer on the surface has been also found which may account for the expected volatilization of this element in the surface of the film during processing.

Unlike BNBT stoichiometric thin films, the experimental RBS curves of the BNBTxs5.5, BNBTxs10.0 and BNBTxs15.0 films show a gradual increasing of the intensity at around 1400 keV, (Figure 2 d-f). In these films, the calculations show that the Bi_xPt interfaces are much thicker (> 10%, Table I) than those of the BNBT films. A bismuth gradient seems to occur in the BNBTxs films, with a Bi-concentration increase from the surface to the substrate (Figure 2). The bulk layer of these films has an

average composition per atom with x values that differ from the nominal ones, ~0.055, ~0.120 and ~0.135, when the expected x values are 0.055, 0.100 and 0.150 (Table I). Moreover, the thickness of the bulk perovskite layer simulated in these BNBTxs films has an average value of ~80 % of the total film thickness, far from the average value of ~90% calculated for the BNBT films. Besides, a pure platinum layer, without bismuth contamination does not give a reliable fit, indicating the massive interdiffusion generated in the BNBTxs films.

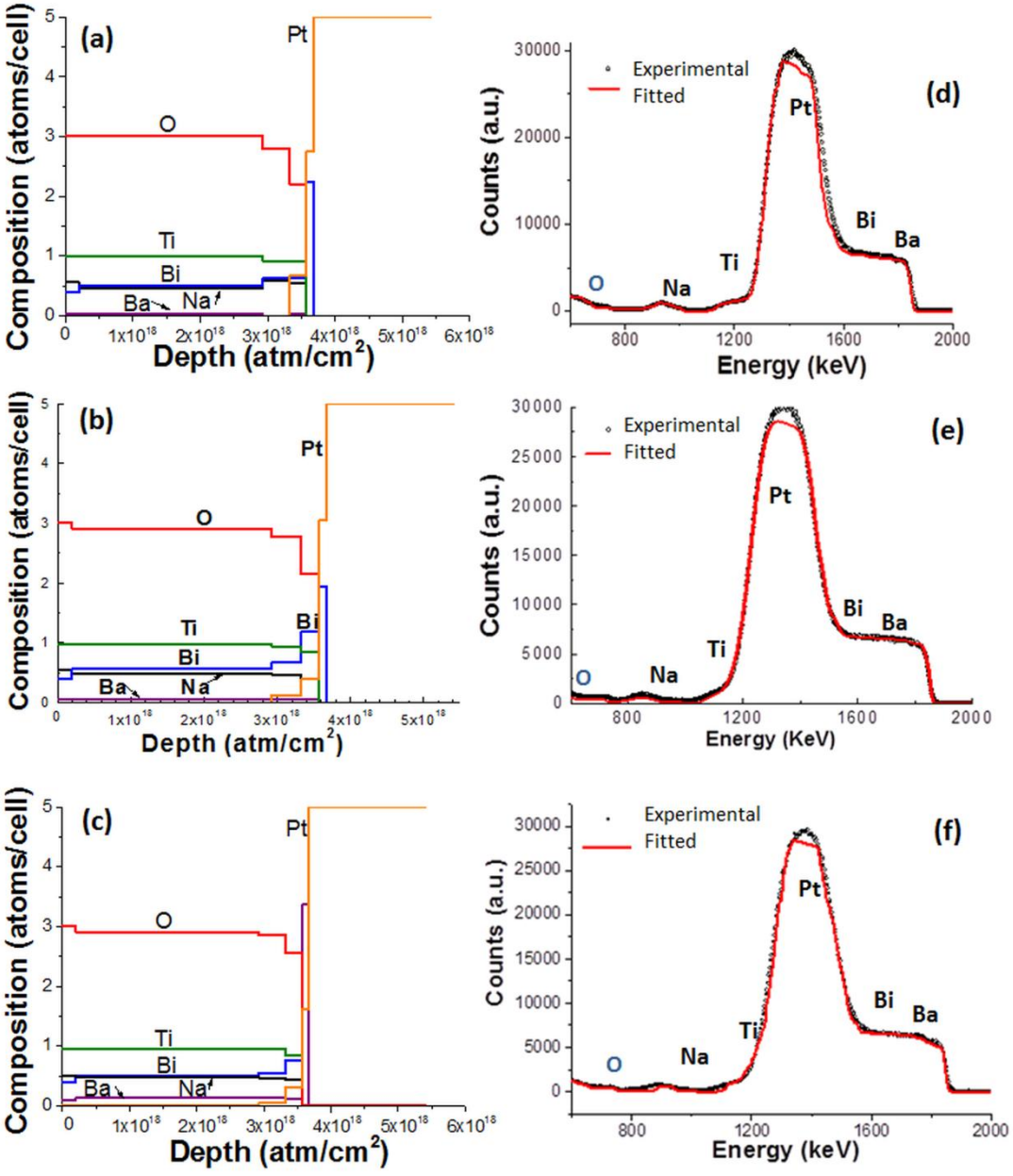

Figure 1. Compositional depth profiles of the BNBT thin films (stoichiometric samples), calculated from the RBS experimental curves, for the (a) BNBT3.5, (b) BNBT5.5 and (c) BNBT10.0 thin films on Pt-coated silicon substrates. The experimental (dotted black line) and fitted (solid red line) RBS spectra for (d) BNBT3.5 (e) BNBT5.5 (f) BNBT10.0 films

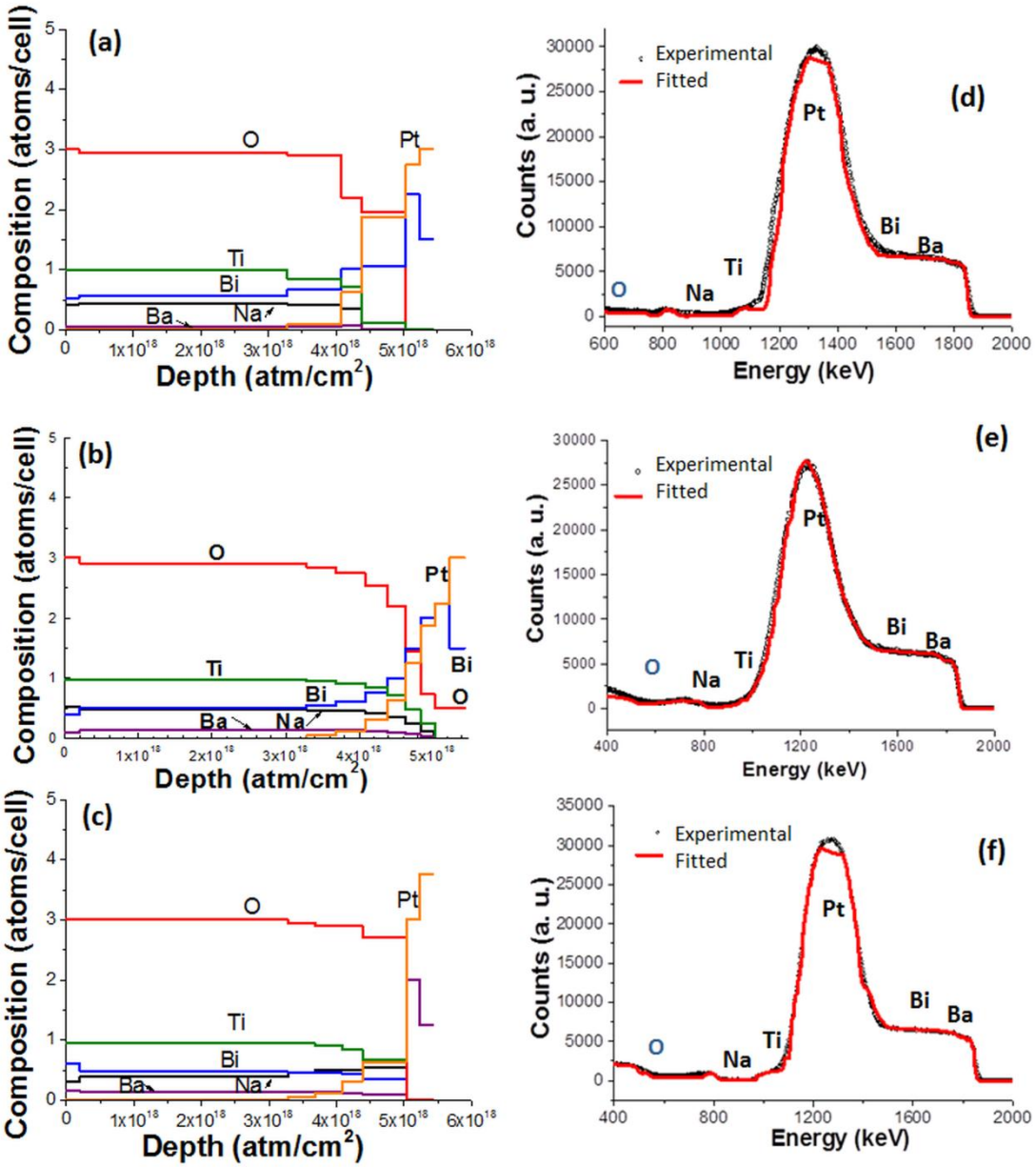

Figure 2. Compositional depth profiles of BNBTxs thin films (samples with Na(I) and Bi(III) excesses), calculated from the RBS experimental curves, for the (a) BNBTxs5.5 , (b) BNBTxs10.0 and (c) BNBTxs15.0 thin films on Pt-coated silicon substrates. The experimental (dotted black line) and fitted (solid red line) RBS spectra for (d) BNBTxs5.5 (e) BNBTxs10.0 (f) BNBTxs15.0 films

Figure 3 shows the FEG-SEM micrographs of BNBT and BNBTxs thin films onto $Pt/TiO_2/SiO_2/Si(100)$ (plan-view and cross section images). Thicknesses of the BNBT3.5, BNBT5.5 and BNBT10.0 films obtained from these micrographs (Figure 3 a-c at the bottom) are collected in Table I and show good agreement with those calculated from the RBS data. The BNBT5.5 film exhibits a low porosity on the surface and a dense microstructure across the film, with well-defined grains of ~110 nm. The BNBT3.5 and BNBT10.0 films show a higher porosity on the surface and across the sample, with slightly smaller grains of ~70 nm (Figure 3 a-c at the top). However, the microstructures of the BNBTxs films are more heterogeneous, with high porosity along the entire film thickness (Figure 3 d-f at the top). Thicknesses calculated from the

cross-section micrographs (Figure 3 d-f at the bottom) are collected in Table I. In this case, most probably due to the appearance of a thicker interface with the substrate that may distort the thickness estimations from RBS data, the thickness values obtained by FEG-SEM differ significantly from those of the RBS data, around 10%. A larger grain size is observed for BNBTxs5.5 (~100 nm) compared with those of the BNBTxs10.0 and BNBTxs15.0 films (~90 nm and ~80 nm, respectively).

Table I. RBS data for BNBT and BNBTxs thin films. The total thickness of the simulated layers (atom/cm^2) up to 60% of Pt content is used to calculate the percent of the surface, bulk and interface thicknesses of each sample. The densities calculated from the crystallographic perovskite data obtained from the corresponding XRD patterns of the BNBT and BNBTxs films are considered to calculate the thicknesses from the RBS curves. Error in the composition calculated by RBS is 10%. Errors in the thicknesses calculated from RBS and SEM are 5%. The RBS regions considered for the calculations are: (i) a bismuth deficient layer on the surface (ii) a bulk layer with a composition close to that of the nominal perovskite (in the nominal composition column) and (iii) a film-substrate interface layer with a composition close to the Bi_xPt alloy

		Data from RBS analysis		Thickness (nm) calculated from RBS and SEM		
Sample	**Nominal composition**	**Areas**	**% of the total thickness**	**RBS**	**SEM**	**Differ. (%)**
BNBT3.5	$(Bi,Na)_{0.965}Ba_{0.035}TiO_3$	Surface deficient on Bi Bulk:$(Bi,Na)_{0.965}Ba_{0.035}TiO_3$ Interlayer $Bi_{0.82}Pt$	4 90 6	346	364	5
BNBT5.5	$(Bi,Na)_{0.945}Ba_{0.055}TiO_3$	Surface deficient on Bi Bulk:$(Bi,Na)_{0.945}Ba_{0.055}TiO_3$ Interlayer $Bi_{0.64}Pt$	5 92 3	330	341	3
BNBT10.0	$(Bi,Na)_{0.900}Ba_{0.100}TiO_3$	Surface deficient on Bi Bulk:$(Bi,Na)_{0.950}Ba_{0.100}Ti_{0.95}O_3$ Interlayer $Bi_{0.48}Pt$	3 93 4	430	435	1
BNBTxs5.5	$(Bi,Na)_{1.040}Ba_{0.055}TiO_{3.095}$	Surface deficient on Bi Bulk:$(Bi,Na)_{1.069}Ba_{0.055}Ti_{0.95}O_{2.93}$ Interlayer $Bi_{0.64}Pt$	5 80 15	482	559	14
BNBTxs10.0	$(Bi,Na)_{0.990}Ba_{0.100}TiO_{3.095}$	Surface deficient on Bi Bulk:$(Bi,Na)_{1.005}Ba_{0.12}Ti_{0.98}O_{2.92}$ Interlayer $Bi_{0.32}Pt$	4 85 11	484	553	13
BNBTxs15.0	$(Bi,Na)_{0.925}Ba_{0.150}TiO_{3.095}$	Surface deficient on Bi Bulk:$(Bi,Na)_{0.904}Ba_{0.135}Ti_{0.96}O_3$ Interlayer $Bi_{0.44}Pt$	10 74 16	513	560	8

Firstly, the structure of the BNBT bulk ceramics has first been studied in order to assess the space groups of the phases developed in the BNBT materials of this work. X-ray diffractograms of the BNBT3.5, BBT5.5 and BNBT10.0 bulk ceramics (Figure 4) clearly illustrate the splitting of the reflections assigned to the tetragonal or/and rhombohedral phases (Figure 4 b and c). The broadening of the peaks in thin films, as observed in the X-ray patterns of Figure 5, caused by small grains and stresses induced by the substrate does not allow us to distinguish this splitting.

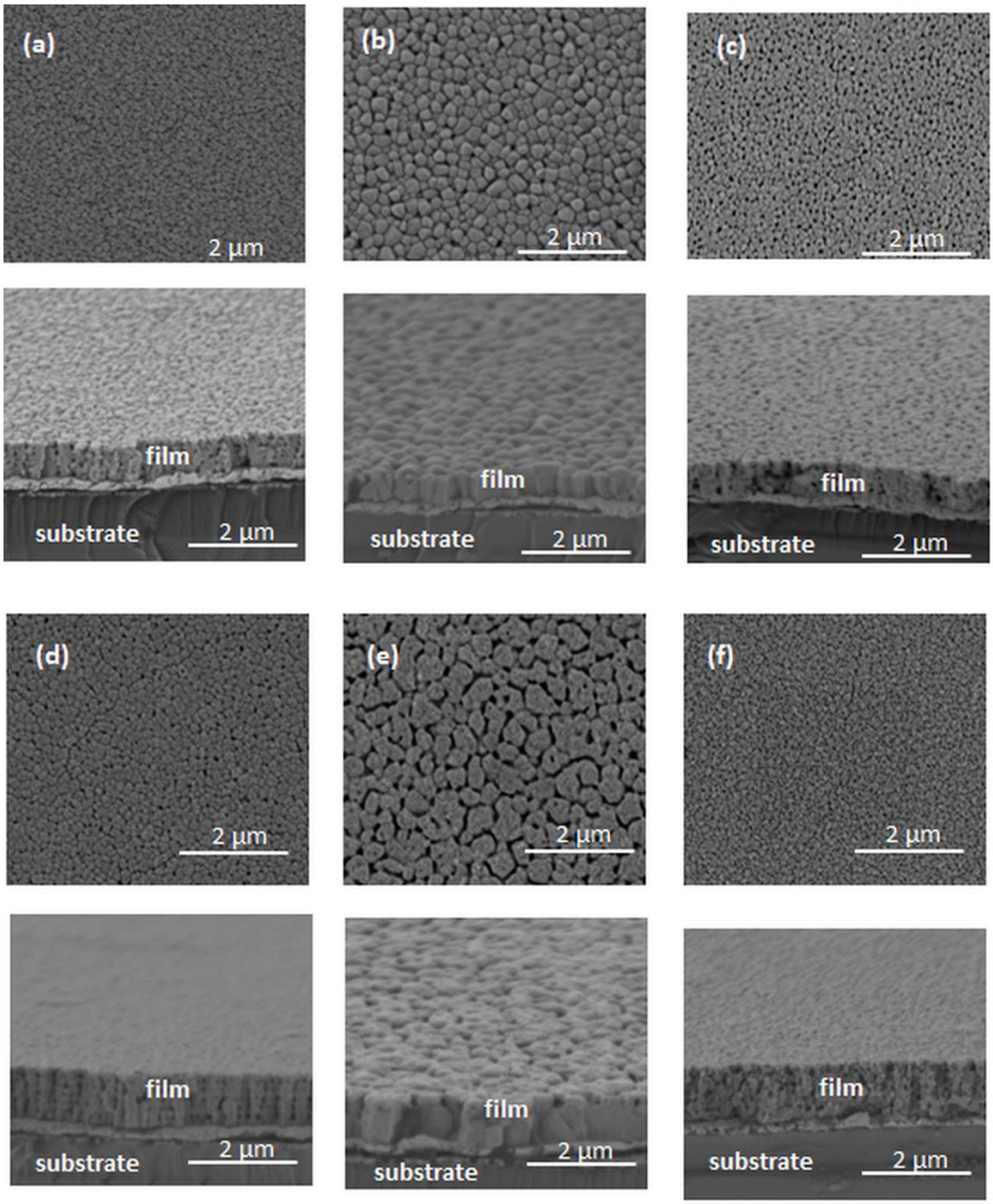

Figure 3. FEG-SEM plan views (at the top) and cross-section images (at the bottom) of the BNBT and BNBTxs films crystallized at 650°C: (a) BNBT3.5 (b) BNBT5.5, (c) BNBT10.0 (d) BNBTxs5.5 (e) BNBTxs10.0 (f) BNBTxs15.0

The XRD pattern of BNBT3.5 bulk ceramic was obtained and interpreted to be used as a reference in the study of the related thin films. The crystalline structure of the bulk ceramic of this composition is presently associated with the rhombohedral R3c space group [29] or to the monoclinic Cc group [30]. In the diffraction experiments, the differences emerging from the mentioned models are subtle. For the resolution and counting statistics of our experiment, the R3c model works satisfactorily.

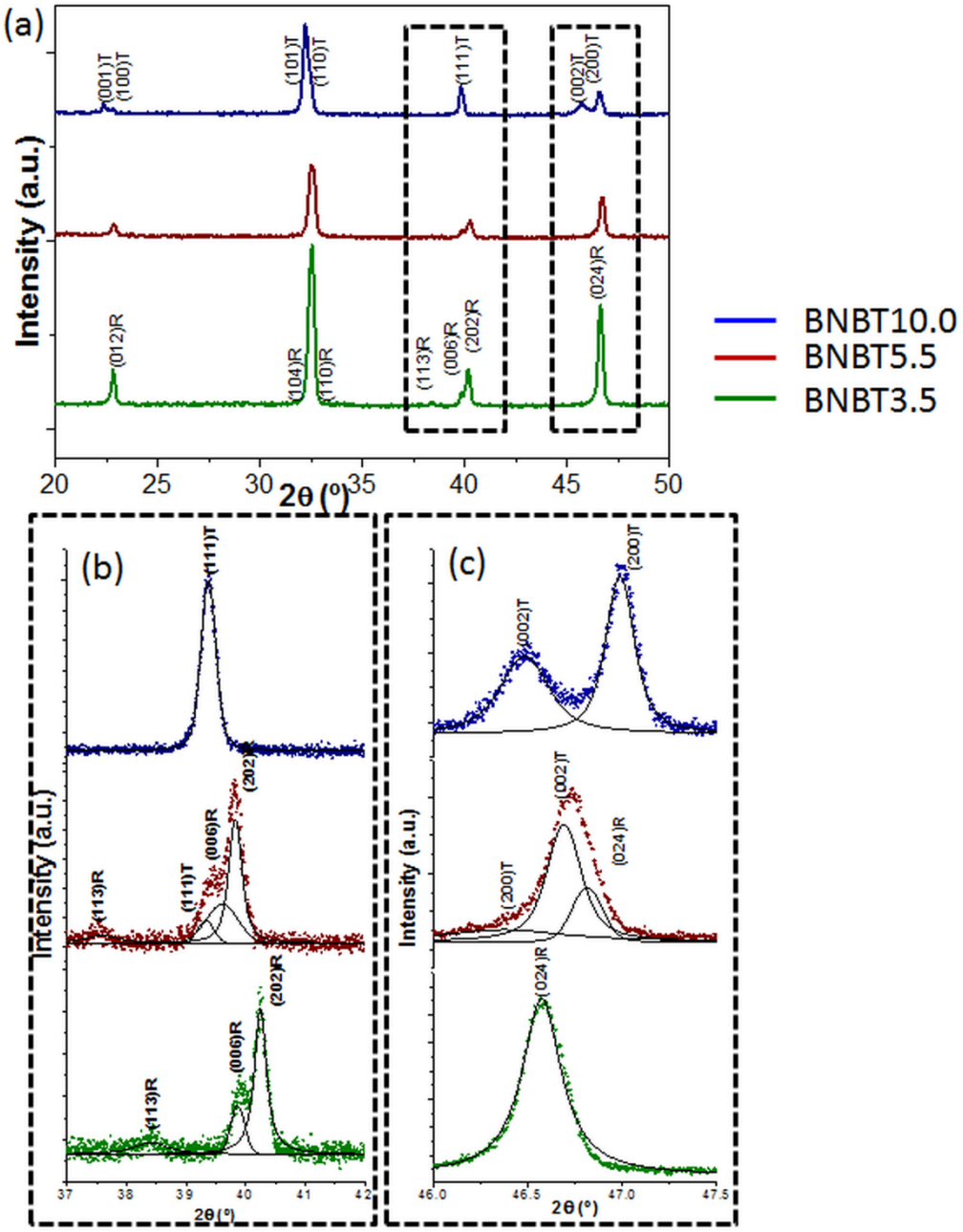

Figure 4. XRD patterns of BNBT3.5, BNBT5.5 and BNBT10.0 bulk ceramics: (a) 2θ values from 20.0° to 50.0° with a step of 0.05° per each 3 seconds (b) 2θ values from 37.0° to 42.0° and (c) 2θ values from 46.0° to 47.5°, both with a step of 0.005° per each 5 seconds

In the case of the tetragonal BNBT10.0 bulk ceramic, the doublets centered at 2θ~22.1° and 2θ~46.8°, ascribed to the (001)/(100) and (002)/(200) reflections, respectively, are characteristic of a tetragonal P4mm space group (Figure 4 a and c, at the top).

The XRD analysis of these ceramics confirms that the MPB is around x = 0.055, where the coexistence of phases is observed (Figure 4 a-c, patterns in the middle).

The XRD patterns of the films in a powder diffractometer (Figure 5) only exhibit pseudocubic-like signature of the parent perovskite phase. As expected for thin films, broad peaks are observed [31]. The symmetrical-centered pseudo-cubic phase detected in these patterns would not explain the piezo-ferroelectric behavior reported for these films [32-35]. Thus, a much more detailed structural analysis is needed to get deeper knowledge on the structural characteristics of these films, the reason why we complemented our measurements using four-circle diffractometry and grazing-incidence X-ray diffraction (GIXRD) with synchrotron radiation.

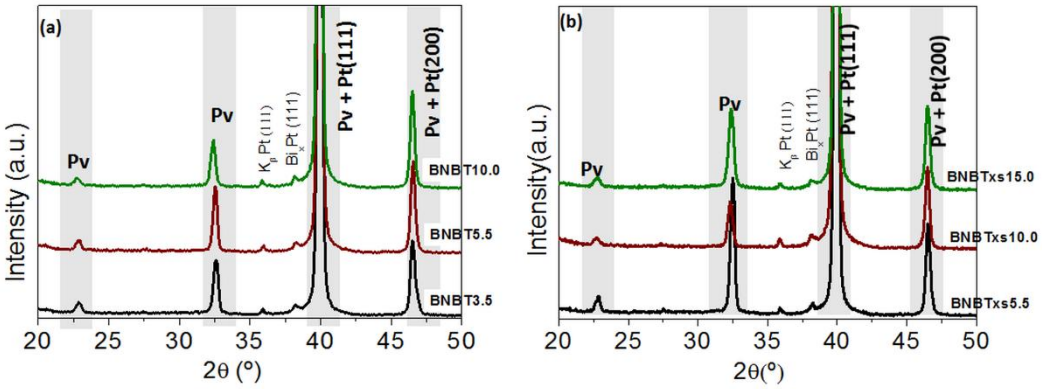

Figure 5. XRD patterns of the (a) BNBT stoichiometric thin films and (b) BNBTxs thin films, containing Na(I) and Bi(III) excesses. Pv indicates the reflections ascribed to the perovskite phase

Four-circle diffractometry (Figure 6 and Figure 7) offers the possibility to collect a large number of patterns in as many sample orientations as necessary to ensure suitable structural refinement. Thus, we used the sum diagram for Rietveld refinement. Such a sum diagram reduces considerably the textural effects associated with both the film (only briefly considered here) and <111> Pt coated silicon substrate. Figure 6 shows the good refinement quality obtained on such summed diagrams. The lattice parameters and the volume fraction of each phase obtained from the Rietveld refinement of the patterns are shown in Table II. The goodness-of-fit (χ^2) always show values close to 1, which confirms the reliability of the refinements.

For the calculations, R3c space group for the rhombohedral phase and P4mm for the tetragonal one have been chosen. They have been identified in the analysis of the XRD data of their corresponding bulk ceramics above (Figure 4). Previous studies have reported alternative space groups for BNBT materials: R3m for the rhombohedral phase, P4bm for the tetragonal, and the monoclinic Cc symmetry as an averaged 'best fit' of the aforementioned phases [7,12,**15**,16, 29-30]. Our calculations show that the use of these space groups produce worse adjustment than the refinements carried out assuming the R3c space group for the rhombohedral and the P4mm space group for the tetragonal phase. Reflections corresponding to the Pt are fitted to a cubic structure ($Fm\bar{3}m$). In the case of BNBT5.5 and BNBTxs10.0 samples, a low reliability is obtained for the refinement to a tetragonal (P4mm) or rhombohedral (R3c) structure separately (Figure 7). However, the adjustment using both phases, what is distinctive of the MPB, give a better fit reliability (Figure 6 b and e, Table II). The lattice parameters found for the two phases do not vary significantly, neither when the phases coexist in the film nor

when excesses are used in the precursor solutions. Also the relative content of the two phases in the films showing phase coexistence are not very different, showing always a large percentage of the rhombohedral phase.

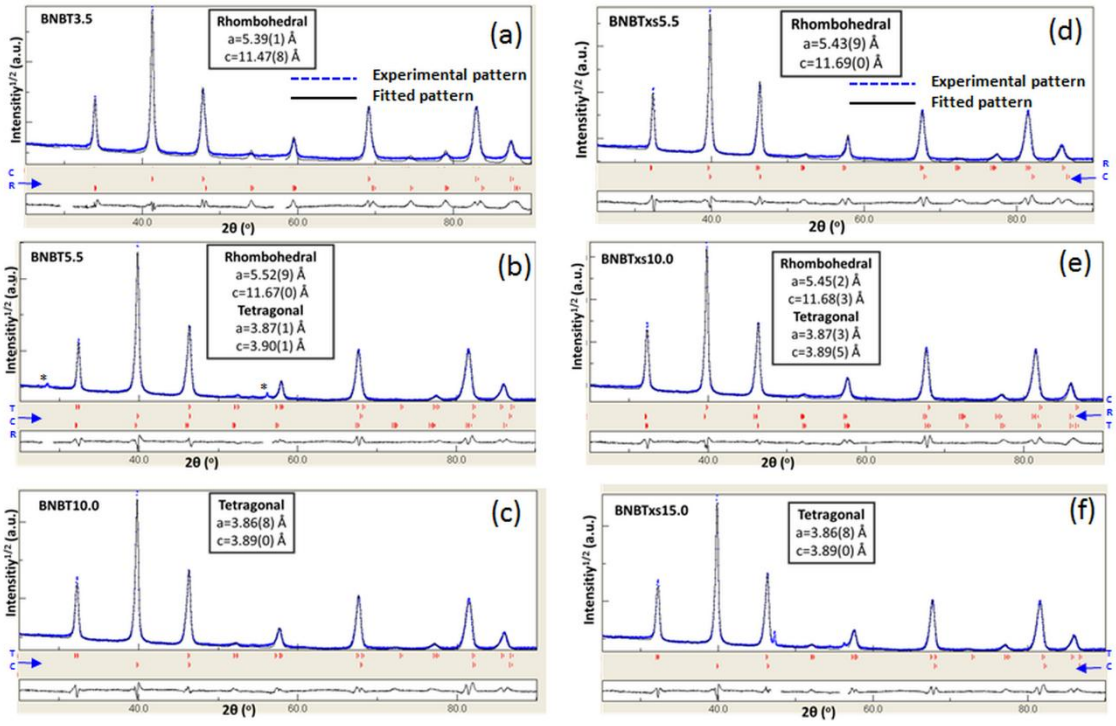

Figure 6. Experimental (blue dotted line) and fitted (black solid) XRD patterns summed over sample orientations for BNBT (a-c) and BNBTxs (d-f) thin films. * indicates peaks associated with the sample holder

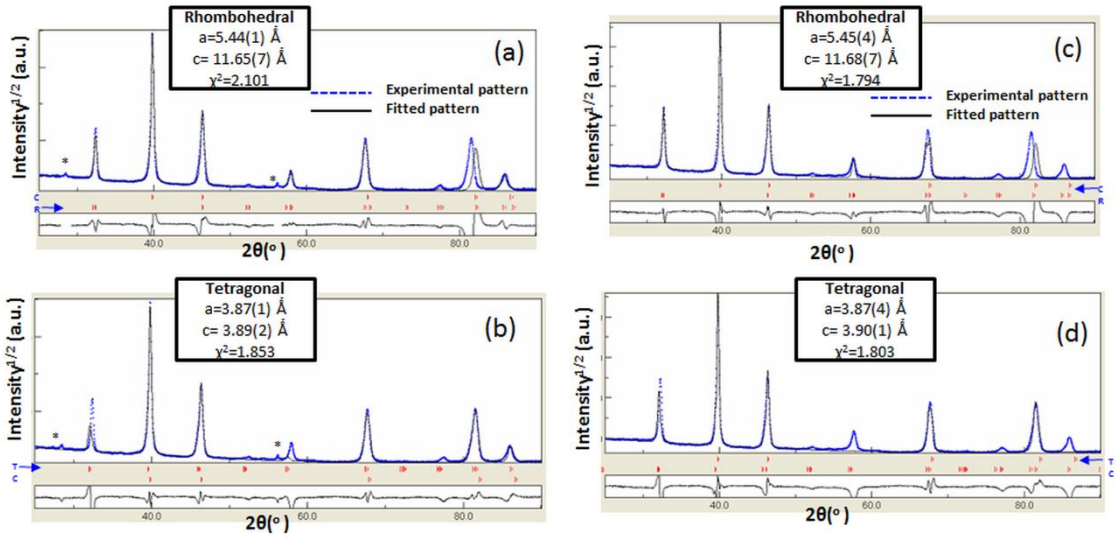

Figure 7. Experimental (blue dotted line) and fitted (black solid) XRD patterns summed over sample orientations for BNBT5.5 (a-b) and BNBTxs10.0 (c-d) thin films. The refinements are performed in the experimental profiles using exclusively the rhombohedral or the tetragonal phases used in the adjustments of figure 6. * indicates peaks associated with the sample holder. The goodness-of-fit (χ^2) are included for each refinement

Table II. Data calculated using a Rietveld refinement of the experimental summed XRD patterns recorded for the BNBT and BNBTxs thin films, using a four-circle diffractometer

Sample	Phase	Space group	a_R or a_T(Å)	c_R or c_T(Å)	Cell volume (Å^3)	Mass per unit cell (g)	Density (g/cm^3)	χ2	Volume fraction (%)
BNBT3.5	Rhombohedral	R3c	5.39	11.48	289	$2.06 \cdot 10^{-21}$	7.127	1.110	99.90
BNBT5.5	Tetragonal	P4mm	3.87	3.90	59	$3.57 \cdot 10^{-22}$	6.065	1.120	29.00
	Rhombohedral	R3c	5.52	11.67	308	$2.14 \cdot 10^{-21}$	6.956		71.00
BNBT10.0	Tetragonal	P4mm	3.87	3.89	59	$3.63 \cdot 10^{-22}$	6.192	1.176	99.00
BNBTxs5.5	Rhombohedral	R3c	5.44	11.69	300	$2.16 \cdot 10^{-21}$	7.195	1.190	99.00
BNBTxs10.0	Tetragonal	P4mm	3.87	3.90	59	$3.69 \cdot 10^{-22}$	6.274	1.201	18.00
	Rhombohedral	R3c	5.45	11.68	300	$2.22 \cdot 10^{-21}$	7.375		82.00
BNBTxs15.0	Tetragonal	P4mm	3.87	3.89	58	$3.68 \cdot 10^{-21}$	6.321	1.158	99.40

An important matter on resolving the crystalline structure of BNT bulk materials is due to the reported low distortion with respect to a cubic perovskite of both, tetragonal and rhombohedral phases, which coexist in the MPB of this compound [15, 36]. The incorporation of BT to the BNT solid solution increases significantly the distortion of the perovskite cell in [111] (rhombohedral distortion) and [100] (tetragonal distortion). This is observed by a clear splitting of the reflections detected in the bulk ceramics of this work with a conventional source of X-ray (Figure 4). Moreover, the structural study is much more complicated in thin films, because of the characteristic broadening of the diffraction peaks collected by X-ray diffraction in polycrystalline thin films. Therefore, the use of more powerful tools of characterization is demanded for the study of the crystalline structure of these materials in thin film form. Grazing-incidence X-ray diffraction (GIXRD) using synchrotron radiation is used here because it allows us to evaluate possible structural differences in the film depth. In fact, variations of the incidence angle permit the characterization of structural changes from the surface to the bulk of the films. In addition, the high flux of photons of this source makes possible to detect the presence of phases with a low-concentration in the films. However, grazing incidence produces an additional instrumental broadening of the diffraction peaks and thus, the resolution in the cell size is lower than that expected for a synchrotron source where a grazing incidence would not be used.

The 2D diffraction patterns obtained with incident angles ω of 0.05^o and 0.15^o, are shown in Figure 8 (BNBT5.5 film) and Figure 9 (BNBTxs10.0 film), together with their respective 1D patterns obtained by integration of the Debye-Sherrer rings. The Rietveld profile refinements are also shown in the latter. The 2D patterns only show the presence of the perovskite structure from the films and a cubic phase from the Pt substrate. Reflections corresponding to the Pt are fitted to a cubic structure ($Fm\bar{3}m$) with a cell size of 3.90(7) Å (Figure 8) and 3.89(5) Å (Figure 9). The peak with the highest intensity in all patterns is that recorded at $2\theta \sim 20^o$, which corresponds to the (110/101) perovskite reflections of the BNBT film. The lattice parameters and

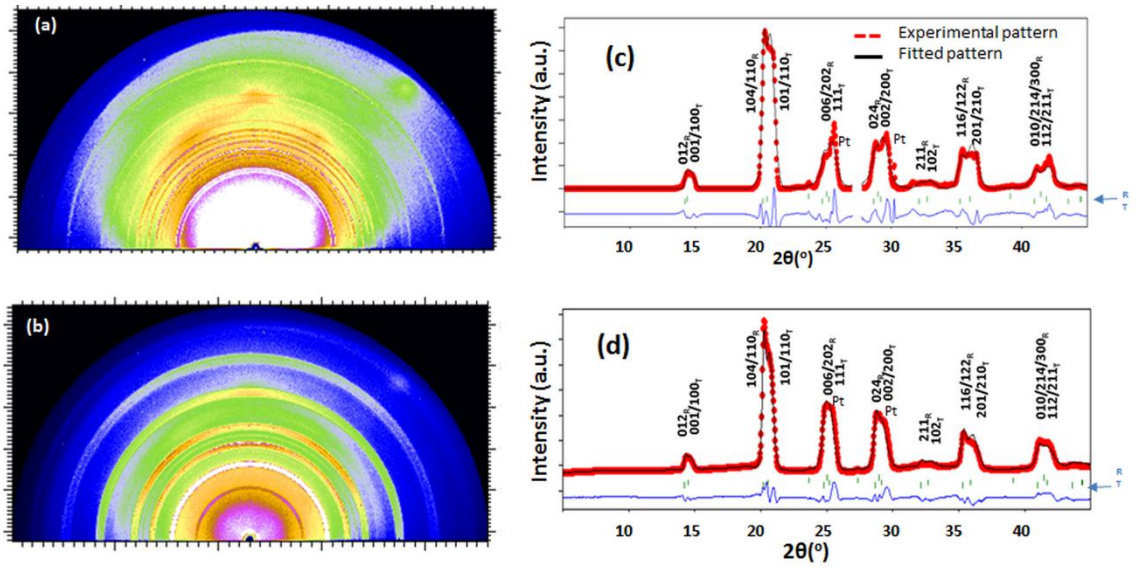

Figure 8. Synchrotron radiation grazing-incidence scattering of the BNBT5.5 thin film. Experimental 2D diffraction patterns are measured with incident angles of (a) ω =0.05^{o} and (b) ω =0.15^{o}. (c) and (d) show the 1D patterns obtained by integration of the corresponding 2D patterns with their Rietveld refinements. Interval from 27.03^{o} to 27.74^{o}, which presents a reflection associated with the sample holder, has been excluded for the fit of 1D pattern recorded at ω =0.05^{o}. R and T indicate rhombohedral and tetragonal structures, which are ascribed to the perovskite phase. Pt indicates the (111) and (200) reflections of the Pt substrate at 25^{o} and 29^{o}

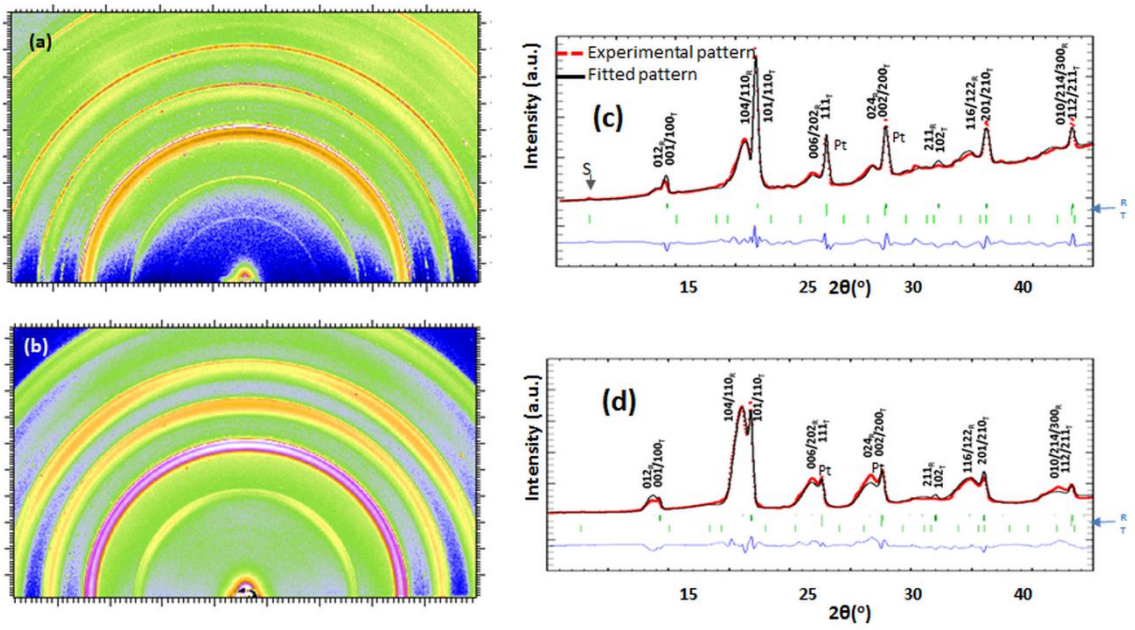

Figure 9. Synchrotron radiation grazing-incidence scattering of the BNBTxs10.0 thin film. Experimental 2D diffraction patterns are measured with an incident angle of (a) ω= 0.05^{o} and (b) ω= 0.15^{o}. (c) and (d) show the 1D patterns obtained by integration of the corresponding 2D patterns with their Rietveld refinements. R and T indicate rhombohedral and tetragonal structures, which are ascribed to the perovskite phase. Pt indicates the (111) and (200) reflections of the Pt substrate at 25^{o} and 29^{o}. A peak associated with a secondary pyrochlore phase (S) is observed in the pattern (c)

percentage of phases of these films, obtained from the refinement of the GIXRD profiles, are shown in Table III.

Table III. Data calculated from the Rietveld refinements of the synchrotron radiation grazing-incidence patterns (λ= 0.9744 Å) of Figures 8 and 9, corresponding to the BNBT5.5 and BNBTxs10.0 thin films, respectively, and at two different incident angles, ω =0.05^o (surface of the film) and ω =0.15^o (bulk film)

	BNBT5.5		**BNBTxs10.0**	
Incident angle (^{o})	0.05		0.05	
Crystal system	Rhombohedral	Tetragonal	Rhombohedral	Tetragonal
Space group	R3c	P4mm	R3c	P4mm
a_R(Å) / a_T (Å)	5.39(8)	3.93(0)	5.64(0)	3.90(5)
c_R(Å) / c_T(Å)	11.85(9)	3.94(3)	12.16(2)	3.91(5)
Volume fraction (%)	79.(0)	21.(0)	41.(8)	58.(2)
Incident angle (^{o})	0.15		0.15	
Crystal system	Rhombohedral	Tetragonal	Rhombohedral	Tetragonal
Space group	R3c	P4mm	R3c	P4mm
a_R(Å) / a_T (Å)	5.43(3)	3.94(0)	5.67(4)	3.90(5)
c_R(Å) / c_T(Å)	11.74(0)	3.93(9)	12.01(5)	3.91(5)
Volume fraction (%)	72.(0)	28.(0)	88.(9)	11.(1)

For the BNBT5.5 film, secondary phases are not detected on any of the diffraction patterns (Figure 8), neither those showing more superficial information of the films (ω=0.05^o) nor those containing more information from the bulk (ω=0.15^o). The relative contents of rhombohedral and tetragonal phases are not significantly different when the incident angle is changed (Table III), and they are similar to the values obtained by using four-circle diffractometry (Table II). The differences observed for the lattice parameters are within the error of the calculations, thus proving the structural homogeneity across the film thickness for samples prepared from solutions without excesses. However, for the BNBTxs10.0 film, a small peak ascribed to a secondary pyrochlore phase is observed at 2θ ~ 9^o in the pattern measured at the lowest incident angle (ω=0.05^o). This suggests the presence of a secondary phase at the surface of the film (Figure 9 c) as the relative intensity of this peak decreases as the incident angle increases (Figure 9 d). In addition, the relative contents of the rhombohedral and tetragonal phases substantially change with the incident angle. The results show that when the volume of material analyzed is more superficial, the rhombohedral phase represents a ~42%, increasing to ~89% when the X ray analysis involves the total volume of the bulk of the film. This percentage is even above the one obtained previously (Table II). Apart from these results that show the inhomogeneity of the films prepared from solutions with excesses, the cell parameters seem not be significantly affected and only variations within the error of the calculations are observed.

Discussion

The RBS curves of the BNBTxs films show that an interdiffusion process, specially ascribed to the bismuth, occurs. This is inferred from a discontinuity in the concentration values from one simulated layer to another (Figure 2). This fact is related to the incorporation of bismuth excesses in the precursor solutions of such films. The increase of bismuth from the surface to the substrate in the BNBTxs films (Table I) can be due to the reactivity of bismuth and platinum, already observed in other reported works concerning $(Bi_{0.50}Na_{0.50})_{1-x}Ba_xTiO_3$ films prepared by CSD and films of other Bi-containing compounds [26, 37]. This is because bismuth forms the Bi_2Pt eutectic and other Bi_xPt alloys [37, 38]. In fact, a small diffraction peak is detected at $2\theta \sim 38^o$ in the XRD diagrams recorded in a powder diffractometer (Figure 5 b), which could be ascribed to a Pt-Bi intermetallic. This reflection cannot be observed in the XRD patterns recorded with a grazing-incidence configuration (Figures 8 and 9) since X-ray penetration is not enough to give valuable information of the interface at the bottom. As XRD patterns recorded with a four-circle diffractometer (Figure 6) collect the sum of those obtained for each (χ, φ) angular position, the texture effects of the possible Bi_xPt intermetallic are also minimized; thus, reflections coming from the intermetallic Bi_xPt are not detected in these XRD diagrams either. Typically, using excesses of volatile elements is considered a method to counterbalance the losses produced during the heating process of thin films [39, 40]. In addition, these excesses hinder the formation of secondary phases, which negatively affect the properties of the material [41-42]. However, the crystallization temperature here employed for the $(Bi_{0.50}Na_{0.50})_{1-x}Ba_xTiO_3$ films seems not to cause a significant volatilization of bismuth. Since this bismuth excess is not incorporated into the perovskite structure, it is able to react with the Pt-coated substrate, producing an appreciable film-substrate interface (Table I).

For the BNBT stoichiometric films, the small fluctuations in the composition across the film thickness, as calculated by RBS, reveal a homogenous compositional depth profile (Figure 1). Furthermore, narrow Bi_xPt film-substrate interfaces are formed, as inferred from the abrupt increase of the intensity at the energy associated with the platinum cross section (~1400 keV) (Figure 1). Therefore, excesses of the volatile elements seem not to be required for the preparation of $(Bi_{0.50}Na_{0.50})_{1-x}Ba_xTiO_3$ films with homogeneous compositional depth profiles.

Concerning the structural characteristics of the $(Bi_{0.50}Na_{0.50})_{1-x}Ba_xTiO_3$ of this work, coexistence of tetragonal and rhombohedral phases, distinctive of the MPB region, is observed for a x value of 0.055 in both bulk ceramics and stoichiometric thin films (Figure 4 and Figure 6b), in accordance with data reported in the literature [17, **18**, 43]. The existence of the two structures would facilitate the polarization rotation and subsequently it might produce an improvement of the piezoelectric response [44, 45].

The MPB in the BNBTxs films is detected for x values of ~0.010. This shift of the MPB towards larger amount of BT observed in this set of samples with excesses has been related [22-25] to the extrinsic effect of a thin film conformation (e.g. strain). As obtained from the RBS study, bismuth excesses (probably also sodium that is not detected by RBS) are not volatilized from the film during the annealing process and, thus, the observed shift could be due to the incorporation of these bismuth excesses into the perovskite structure. This implies that some titanium should be transferred from the BT phase to BNT phase in the solid solution, leaving free oxides, such as BaO. In

addition, excesses of bismuth or sodium that are not incorporated into the perovskite could react among them and with free BaO, giving rise to minor secondary phases, not easily detected by X-ray diffraction. Note that such phases are observed only at the surface of the BNBTxs10.0 film in the GIXRD patterns collected with synchrotron radiation, and only via a small reflection associated with a pyrochlore phase (Figure 9c). The content of this phase is so low that laboratory measurements do not make possible the detection of this crystalline phase (Figure 5b and Figure 6e).

The bismuth deficient layer on the surface of both the BNBT and the BNBTxs films evidences that, although obtaining average values of this deficient layer, ~4% and ~7%, respectively, almost in the error range of the measurement, some loss of volatile elements probably occurs at the top surface of the films during annealing (Table I). However, the results also indicate that excesses of bismuth in these films are not needed to compensate losses by volatilization during annealing; on the contrary, they generate thick bottom interfaces (an average interface thickness of ~14% of the total film thickness in BNBTxs) and secondary phases. Therefore, the use of BNBT solutions with the stoichiometric ratios of the metal cations makes possible the synthesis of thin films with profile compositions close to the nominal one. Additionally, an abrupt bottom interface is developed in these films with an average percentage of thickness of ~4%, which is a clear indication of a low interdiffusion between the film and the substrate (Table I)**.**

GIXRD analysis of the BNBT5.5 and BNBTxs10.0 films using synchrotron radiation corroborates the results obtained by four-circle diffractometry. Peak asymmetries and splittings in the 1D GIXRD patterns (detected as doublets and triplets at 2θ ~20^o, 25^o, 30^o, 36^o and 42^o) demonstrate the formation and coexistence of a rhombohedral and a tetragonal structure in both films, thus indicating that these films are in the MPB (Figure 8 and Figure 9).

For the BNBTxs10.0 film, the intensities associated with the $(012)_R$ and $(001)/(100)_T$; $(104)/(110)_R$ and $(101)/(110)_T$; $(006)/(202)_R$ and $(111)_T$; $(024)_R$ and $(002/200)_T$ peaks are reversed in the GIXRD pattern at $\omega=0.05^o$ comparing with those measured at $\omega=0.15^o$ (Figure 9). However, in the GIXRD patterns of the BNBT5.5 film, the intensities seem not to change from the top surface to the bulk film (Figure 8). This could be ascribed to a higher A-site occupational disorder of the perovskite in the BNBTxs10.0 film due to excesses [46,47]. Moreover, the presence of secondary phases on the surface (Figure 9c) and the large variations of the volume fraction of each phase from the top to the substrate in the BNBTxs10.0 film (Table III) indicate structural heterogeneity for this film.

Deviations in thicknesses obtained by the comparison of thicknesses measured from the FEG-SEM micrographs and calculated from the RBS curves in BNBTxs films may have several causes: the thicker interfaces and inhomogeneous compositional profiles detected by RBS, the inhomogeneous structural profiles determined by GIXRD with synchrotron radiation and the higher porosity. Actually, the high porosity of BNBTxs films observed in the SEM micrographs (Figure 3) could be formed during the volatilization of the excesses of Na(I) and Bi(III), which would explain the denser microstructures of the BNBT films.

In spite of the local complex structure of this system [15], the crystalline structure at large-scale order has been successful described here for these solution derived $(Bi_{0.50}Na_{0.50})_{1-x}Ba_xTiO_3$ films. In general, the crystalline phases that best fit are in agreement with those reported for most of the works on $(Bi_{0.50}Na_{0.50})_{1-x}Ba_xTiO_3$ bulk materials [7, 20]. Particularly, the structural results here presented for thin film samples in the MPB region, are not so far from those which have described a near-cubic matrix with rhombohedral and/or tetragonal nano-regions [48, 49] and that can also explain the relaxor-ferroelectric behavior reported for these films [32].

Summary

The composition and structure of solution derived $(Bi_{0.50}Na_{0.50})_{1-x}Ba_xTiO_3$ stoichiometric thin films and others containing Na(I) and Bi(III) excesses have been investigated. The incorporation of excesses of the Bi(III) and Na(I) volatile elements in the $(Bi_{0.50}Na_{0.50})_{1-x}Ba_xTiO_3$ precursor solutions does not affect their possible losses during the film processing, a fact presumed to be produced in solution derived thin film materials during the crystallization annealing. On the contrary, Na(I) and Bi(III) excesses in the $(Bi_{0.50}Na_{0.50})_{1-x}Ba_xTiO_3$ films of this work stimulate compositional and structural inhomogeneities. Thick film-substrate interfaces, a bismuth gradient in depth and remarkable differences (from the top to the bottom of the film) in the volume fraction of the rhombohedral and tetragonal phases that coexist at the morphotropic phase boundary are observed in these films. In both $(Bi_{0.50}Na_{0.50})_{1-x}Ba_xTiO_3$ thin films prepared from stoichiometric solutions and their counterpart bulk ceramics, the MPB is placed for values of x close to 0.055. However, the MPB is shifted towards larger x values when excesses are incorporated to the films (BNBTxs). This fact proves that the excesses of the volatile elements in the precursor solutions produce a compositional shift of the solid solution in the derived films, which can explain the movement of the MPB in the BNBTxs films.

The results of this work demonstrate that the chemical solution deposition (CSD) process here reported permits to obtain compositionally and structurally homogeneous $(Bi_{0.50}Na_{0.50})_{1-x}Ba_xTiO_3$ thin films in the MPB region, potentially useful for applications.

Acknowledgements

This work was financed by Spanish Project MAT2013-40489-P. D. Pérez-Mezcua acknowledges the financial support of the FPU Spanish program (AP2012-0639). A portion of this research was carried out at the Stanford Synchrotron Radiation Lightsource, a national user facility operated by Stanford University. D. Chateigner acknowledges the Conseil Régional de Basse Normandie for its partial financial of the four-circles X-ray diffractometer.

References

1. Muralt P. Ferroelectric thin films for micro-sensors and actuators: a review. J. Micromech Microeng 2000;10:136

2. Phelan D, Long X, Xie Y, Ye Z G, Glazer, H. Yokota A M, Thomas P A, Gehring P M. Single Crystal Study of Competing Rhombohedral and Monoclinic Order in Lead Zirconate Titanate. Phys Rev Lett 2007;105:207601
3. Saito Y, Takao H, Tani T, Nonoyama T, Takatori K, Homma T, Nagaya T, Nakamura M. Lead-free piezoceramics. Nature 2004;432:84
4. Takenaka T, Nagata H. Current status and prospects of lead-free piezoelectric ceramics. J Eur Ceram Soc 2005;25[12]:2693
5. Rödel J, Jo W, Seifert K, Antón E, Granzow T, Damjanovic D. Perspectives on the development of lead-free piezoceramics. J Am Ceram Soc 2009;92:1153
6. Trelcat J, d'Astorg S, Courtois C, Champagne P, Rguiti M, Leriche A. Influence of hydrothermal synthesis conditions on BNT-based piezoceramics. J Eur Ceram Soc 2011;31[11]:1997
7. Ma C, Guo H, Beckmand S P, Tan X. Creation and destruction of morphotropic phase boundaries through electrical poling: a case study of lead-free $(Na_{0.5}Bi_{0.5})_{1-x}Ba_xTiO_3$ piezoelectrics. Phys Rev Lett 2012;109:107602
8. Zhang H, Xu P, Patterson E, Zang J, Jiang S, Rödel J. Preparation and enhanced electrical properties of grain-oriented $(Bi_{1/2}Na_{1/2})TiO_3$-based lead-free incipient piezoceramics. J Eur Ceram Soc 2015;35;2501
9. Takenaka T, Maruyama K I, Sakata K. '$Bi_{1/2}Na_{1/2}TiO_3$-$BaTiO_3$ system for lead-free piezoelectric ceramics. Jpn J Appl Phys 1991;30:2236
10. Cao W, Cross E. Theoretical model for the morphotropic phase boundary in lead zirconate–lead titanate solid solution. Phys Rev B 1993;47:4825
11. Rout D, Moon K S, Rao V S, Kang S J L. Study of the morphotropic phase boundary in the lead- free $Na_{1/2}Bi_{1/2}TiO_3$- $BaTiO_3$ system by Raman spectroscopy. J Ceram Soc Jpn 2009;117[7]:797
12. Jo W, Daniels J, Damjanovic D, Kleemann W, Rödel J. Two-stage processes of electrically induced-ferroelectric to relaxor transition in $0.94(Bi_{1/2}Na_{1/2})TiO_3$- $0.06BaTiO_3$. Appl Phys Lett 2013;102:192903
13. Groh C, Jo W, Rödel J. Frequency and temperature dependence of actuating performance of $Bi_{1/2}Na_{1/2}TiO_3$-$BaTiO_3$ based relaxor/ferroelectric composites. J App Phys 2014;115:234107
14. Noheda B, Cox D E, Shirane G, Gonzalo J A, Cross L E, Park S E. A monoclinic ferroelectric phase in the $Pb(Zr_{1-x}Ti_x)O_3$ solid solution. Appl Phys Lett 1999;74:2059
15. Levin I, Reany M. Nano and Mesoscale structure of $Na_{1/2}Bi_{1/2}TiO_3$: A TEM perspective. Adv Funct Mater 2012;22:3445
16. Montero-Cabrera M E, Pardo L, García A, Fuentes-Montero M E, Ballinas-Casarrubias M L, Fuentes-Cobas L E. The Global and Local Symmetries of Nanostructured Ferroelectric Relaxor $0.96(Bi_{1/2}Na_{1/2})TiO_3$-$0.04BaTiO_3$. Ferroelectric 2014;469:50
17. Pitch G, Töpfer J, Hennig E. Structural properties of $(Bi_{0.5}Na_{0.5})_{1-x}Ba_xTiO_3$ lead-free piezoelectric ceramics. J Eur Ceram Soc 2010;30:3445
18. Deluca M, Pitch G, Hoffmann M J,Rechtenbatch A, Töpfer J, Schader FH, Webber K G. Chemical and structural effects on the high-temperature mechanical behavior of (1-x) $Na_{1/2}Bi_{1/2}TiO_3$-x $BaTiO_3$ ceramics. J Appl Phys 2015;117:134110
19. Cordero F, Craciun F, Trequattrini F, Mercadelli E, Galassi C. Phase transitions and phase diagram of the ferroelectric perovskite $(Na_{0.5}Bi_{0.5})_{1-x}Ba_xTiO_3$ by anelastic and dielectric measurements. Phys Rev 2011;B81:144124
20. Jo W, Daniels J E, Jones J L, Tan X, Thomas P A, Damjanovic D, Rödel J. Evolving morphotropic phase boundary in lead-free $(Bi_{1/2}Na_{1/2})TiO_3$-$BaTiO_3$ piezoceramics. J Appl Phys 2011;109:014110
21. Schwartz R W, Schneller T, Waser R. Chemical solution deposition of electronic oxide films. C R Chimie 2004;7:433
22. Alonso-Sanjosé D, Jiménez R, Bretos I, Calzada M L. Lead- free $Bi_{1/2}Na_{1/2}TiO_3$-$BaTiO_3$ ferroelectric thin films in the morphotropic phase boundary composition: solution processing and properties. J Am Ceram Soc 2009;92 [10]:2218

23. Cernea M, Trupina L, Dragoi C, Vasile V S, Trusca R. Structural and electrical characterization of lead- free $Bi_{1/2}Na_{1/2}TiO_3$-$BaTiO_3$ ferroelectric thin films obtained by PLD and RF- PLD. J Alloy Compd 2012;515:166
24. Zhou Z H, Xue J M, Li W Z, Wang J. Ferroelectric and electrical behavior of $Bi_{1/2}Na_{1/2}TiO_3$ thin films. Appl Phys Lett 2004;85:804
25. Bretos I, Alonso- Sanjosé D, Jiménez R, Ricote J, Calzada M L. Evidence of morphotropic phase boundary displacement in lead- free $(Na_{0.5}Bi_{0.5})_{1-x}Ba_xTiO_3$ polycrystalline thin films. Mater Lett 2011;65:2714
26. Pérez-Mezcua D, Sirera R, Bretos I, Ricote, Jiménez R, Fuentes- Cobas L, Escobar-Galindo R, Chateigner D, Calzada M L. Morphotropic Phase Boundary in Solution-Derived $(Bi_{0.5}Na_{0.5})_{1-x}Ba_xTiO_3$ Thin Films: Part I Crystalline Structure and Compositional Depth Profile. J Am Ceram Soc 2014;97 [4]:1269
27. Kotai E. Computer method for analysis and simulation of RBS and ERDA spectra. Nucl Instrum Methods 1994;B 85:588
28. Lutterotti L. Materials Analysis Using Diffraction. http://www.ing.unitn.it/~maud/
29. Fuentes-Cobas L E, Pardo L, Montero-Cabrera M E, Plaisier J R, García A, Brebøl K, Mercadelli E, Galassi C. The $0.96(Bi_{0.5}Na_{0.5})TiO_3 – 0.04BaTiO_3$ crystal structure: A high-Q, high-counting statistics synchrotron diffraction analysis. Cryst Res Technol 2014; 49:190
30. Usher T M, Forrester J S, de la Cruz C R, Jones J L. Crystal structure of 0.96 $0.96(Bi_{0.5}Na_{0.5})TiO_3 – 0.04BaTiO_3$ from combined refinement of X-ray and neutron diffraction patterns. Appl Phys Lett 2012; 101:152906
31. Alguero M, Calzada M L, Pardo L, Snoeck E. Combined effect of grain size and tensile stresses on the ferroelectric properties of sol-gel $(Pb,La)TiO_3$ thin films. J Mater Res 1999;14[12]:4570
32. Pérez-Rivero A, Ricote J, Bretos I, Calzada M L, Pérez de la Cruz J,. Fernández J R A, Jiménez R. Morphotropic phase boundary in solution derived $(Bi_{0.5}Na_{0.5})_{1-x}Ba_xTiO_3$ thin films. Part II Functional properties J Am Ceram Soc 2014;97[4]:1276
33. Rawat M, Yadav K L, Kumar A, Patel P K, Adhlakha N, Rani J. Structural, dielectric and conductivity properties of Ba^{2+} doped $(Bi_{0.5}Na_{0.5})TiO_3$ ceramic. Adv Mat Lett 2012;3[4]:286
34. Anton E M, Jo W, Damjanovic D, Rödel J. Determination of depolarization temperature of $(Bi_{1/2}Na_{1/2})TiO_3$-based lead-free piezoceramics. J Appl Phys 2011;110:094108
35. Daryapurkara S, Koltea J T, Gopalana P. Growth and Characterization of $Na_{0.5}Bi_{0.5}TiO_3$ Thin Films with $BaTiO_3$ Buffer Layer (Study of $Au/Na_{0.5}Bi_{0.5}TiO_3/BaTiO_3/Pt$ Capacitor). Ferroelectrics 2013;447[1]:46
36. Jones G O, Thomas P A. Investigation of the structure and phase transition in the novel A-site distorted perovskite compound $Na_{0.5}Bi_{0.5}TiO_3$. Acta Crys 2002;B58:168
37. Calzada M L, Jiménez R, González A, García-López J, Leinen D, Rodríguez-Castellón E. Interfacial effects and electrical characteristics of ferroelectric strontium bismuth tantalate thin films on Pt/TiO_2 and Ti/Pt/Ti heterostructure electrodes. Chem Mater 2005;17:1441
38. Okamoto H, The Bi-Pt (Bismuth-Platinum) system. J Phase Equilib 1991;12[2]:207
39. Tanaka K, Hayashi H, Kakimoto K, Ohsato H, Iijima T. Effect of (Na,K)-Excess Precursor Solutions on Alkoxy- Derived $(Na,K)NbO_3$ Powders and Thin Films. Jpn. J Appl Phys 2007;46[10B]:6964
40. Ledermann N, Muralt P, Baborowski J, Gentil S, Mukati K, Cantoni M, Seifert A, Setter N. {1 0 0 }-Textured, piezoelectric $Pb(Zrx, Ti_{1-x})O_3$ thin films for MEMS: integration, deposition and properties. Sensors and Actuators A 2003;105:162
41. Liu H, Guo Y, Guo B, Zhang D. Synthesis and visible-light in the photocatalysis capability of $BiFeO_3$- nanopowders by sol-gel method. Solid State Science 2013;19:69

42. Calzada M L, Algueró M, Pardo L. Chemistry-crystallization-microstructure relations of sol-gel derived lanthanum modified lead titanate thin films. J Sol-Gel Sci Technol 1998;13:837
43. Pardo L, Mercadelli E, García A, Brebøl K, Galassi C. Field-Induced Phase Transition and Relaxor Character in Submicrometer Structured Lead-Free $(Bi_{0.5}Na_{0.5})_{0.94}Ba_{0.06}TiO_3$ Piezoceramics at the Morphotropic Phase Boundary. IEEE Trans Ultrason Ferroelectr Freq Control 2011;58[9]:1893
44. Ibrahim A B M A, Murgan R, Rahman M K A, Osman J. Morphotropic Phase Boundary in Ferroelectric Materials. Ferroelectrics- Physical Effects. 2011, Intech, Croatia
45. Damjanovic D. Contribution to the piezoelectric effect in ferroelectric single crystals and ceramics. J Am Ceram Soc 2005;88[10]:2663
46. Kling J, Hayn S, Schmitt L A, Gröting M, Kleebe H J, Albe K. A-site occupancy in the lead-free $(Bi_{1/2}Na_{1/2}TiO_3)_{0.94}$-$(BaTiO_3)_{0.06}$ piezoceramic: Combining first-principles study and TEM. J Appl Phys 2010;107:114113
47. Gomah-Pettry J, Saïd S, Marchet P, Mercurio J P. Sodium-bismuth titanate based lead-free ferroelectric materials. J Eur Ceram Soc 2004;24:1165
48. Montero-Cabrera M E, Pardo L, García A, Fuentes-Montero M E, Ballinas-Casarrubias M L, Fuentes-Cobas L E. The Global and Local Symmetries of Nanostructured Ferroelectric Relaxor $0.94(Bi_{0.5}Na_{0.5})TiO_3$ – $0.06BaTiO_3$. Ferroelectrics 2014;469:50
49. Daniels J E, Jo W, Rödel J, JonesJ L. Electric-field-induced phase transformation at a lead-free morphotropic phase boundary: Case study in a 93%$((Bi_{0.5}Na_{0.5})TiO_3$ – 7%$BaTiO_3$ piezoelectric ceramic. Appl Phys Lett 2009;95:032904